

Label-free microscope for rheological imaging of cells

NICOLAS P. MAURANYAPIN,¹ MARINO LARA ALVA,¹ DANIEL YAN,², ZHE YANG,³, JACKSON D. LUCAS¹, ALEX TERRASSON¹, MICHAEL A. TAYLOR,⁴ ROHAN TEASDALE,³ YUN CHEN² AND WARWICK P. BOWEN^{1,*}

¹ Australian Research Council Centre of Excellence in Quantum Biotechnology (QUBIC), The University of Queensland, Australia

² Department of Mechanical Engineering, Center for Cell Dynamics, Institute for NanoBioTechnology (INBT) Johns Hopkins University, Baltimore, USA

³ School of Biomedical Sciences, The University of Queensland, Australia.

⁴ University of Otago, Dunedin, New Zealand

*w.bowen@uq.edu.au

Abstract: Many essential cellular functions depend on the viscoelastic properties of the cytoplasm. While techniques such as optical tweezers and atomic force microscopy can measure these properties, their reliance on localized probes prevents intracellular imaging and perturbs native cellular behaviour. Label-free microscopy offers a non-invasive alternative for observing intracellular dynamics. However, limitations in signal-to-noise ratio and imaging speed typically restrict analysis to diffusivity, leaving cellular viscous properties inaccessible. Here, we introduce rheoSCAT, a label-free, phase-sensitive microscope engineered with ultra-low phase noise. This system enables measurements of intracellular dynamics at frequencies up to 50 kHz, twenty times faster than previous label-free approaches. Applied to live cancer cells, this technique establishes a connection between label-free microscopy and rheology. The high speed of our technique reveals viscoelastic behaviours that were previously inaccessible, which we show are consistent with probe-based microrheology observations. The rheological images produced distinguish intra- and extracellular regions with high contrast, resolve spatial variations in cellular mechanics, and enable monitoring of cellular state and stress over time. The ability to quantitatively map intracellular energetics and viscoelasticity offers a powerful tool for advancing fundamental cell biology, cancer research, clinical diagnostics, and drug development.

Cell function and health critically depend on the physical properties of the cytoplasm. In particular, cytoplasmic viscoelasticity and dynamics govern essential processes such as intracellular transport, cell motility, and mechanochemical transduction [1]. Alterations in these mechanical properties are associated with chronic inflammation, neurodegenerative diseases, and cancer [1]. Microrheology techniques have been developed to probe cytoplasmic viscoelasticity by tracking the motion of tracer particles – such as micro-beads [2], magnetic rods [3], fluorescent tags [4] or AFM tips [5] – either embedded within the cell or attached to its membrane. These methods have revealed that cells exhibit a complex shear modulus, reflecting both elastic and viscous behaviour dependent on excitation frequency [5–7]. However, the introduction of probe particles can disrupt cellular function or even lead to cell death [8]. More critically, because these techniques rely on tracking of individual particles, they are inherently incompatible with continuous, full-field spatial imaging.

Label-free microscopy techniques are well-suited for imaging applications and offer a non-invasive alternative for probing intracellular mechanics, as they enable detection of the motion of endogenous cellular components without perturbing the sample. Techniques such as Rotating Coherent Scattering (ROCS) [9] and Interferometric Scattering (iSCAT) [10, 11] have

demonstrated exceptional sensitivity—down to the level of single proteins in free solution—and can track their motion over time and diffusivity [12]. However, current implementations of these techniques are constrained by limited acquisition speed and low signal-to-noise ratios, restricting measurements to frequencies below 2.5 kilohertz range inside live-cell environments. This presents a significant limitation and has prevented the connection between the cellular constituents motion and cellular rheology. Notably, the transition and the viscous behaviour typically happen at frequencies larger than kilohertz [5]. Dynamic light scattering [13] and coherent brightfield (COBRI) microscopy [14] are capable of high-frequency measurements; however, their low signal-to-noise ratio has so far impaired their application to intracellular imaging.

Here, we introduce rheoSCAT microscopy, a new label-free technique capable of detecting cellular constituent dynamics and continuously imaging cellular microrheological properties with sub-micron spatial resolution. This is made possible by a 50 kHz bandwidth, achieved through substantial suppression of laser phase noise, enabling the detection of minute phase fluctuations driven by micro- to nanoscale intracellular motion. It allows the observation of both the elastic and viscous response of the cell and the transition between the two regimes. Experiments on living cancer cells demonstrate that the ratio of elastic and viscous modulus can be extracted up to 50 kHz and spatially imaged over the entire field of view. These images provide high contrast between extra- and intracellular environments, uncover spatial features invisible to conventional microscopes, and allow monitoring of cellular state and the effect of stress caused by chemical assault.

The ability of rheoSCAT microscopy to quantitatively image cellular dynamics and microrheology could shed new light on basic biological processes that remain poorly understood, such as intracellular transport [15], energy transfer [16], and the mechanics of cellular signalling [17]. It could also have applications in medical research, contributing to the development of new diagnostic methods, drug discovery, the study of neurodegenerative diseases, and regenerative medicine.

Results

rheoSCAT microscopy

Figure 1a provides a schematic of the rheoSCAT microscope which, like iSCAT [18], harnesses the interference between the scattered light from a specimen and the reflected light from a microscope slide that it is attached to. Upon detection, the interference creates a photocurrent which can be approximated to first order as (see Supplementary Information)

$$i(t) \propto \sqrt{I_r} \left[\underbrace{\sqrt{I_r} + 2\sqrt{I_s}\cos\phi}_{\text{static phase signal}} + \underbrace{\sqrt{I_s}\delta S(t)}_{\text{bioactivity signal}} + \underbrace{2\delta N(t)}_{\text{light noise}} \right] + \underbrace{\delta E(t)}_{\text{electronic noise}}. \quad (1)$$

Here I_r and I_s are the mean intensities of the reflected and scattered fields, respectively, ϕ is the mean phase difference between the two fields, and we have assumed that $I_r \gg I_s$. The first term in Eq. (1) is a static phase signal analogous to the signal from iSCAT [18]. The other terms are associated with fluctuations. δS is the rheoSCAT signal due to cellular constituents fluctuations, δN is the optical noise on the measurement, and δE is the electronic noise of the detection system.

Since the amplitude of cellular fluctuations decreases as a power law with frequency [19], strong noise suppression of both the electronic and light noise is required to observe fast bioactivity signals.

The near-identical optical paths traversed by the reflected and signal fields (see Fig. 1a), with a path difference of around 300 μm , greatly suppresses phase fluctuations generated within the

microscope compared to traditional phase-contrast or DIC microscopes [20]. In addition, as shown in Eq. (1), the interference amplifies the bioactivity signal by a factor of $\sqrt{I_r I_s}$ above the electronic noise floor of the detection system [18, 21]. This greatly suppresses electronic noise so that light-noise limited detection is possible using a high bandwidth photoreceiver rather than a lower noise, lower bandwidth alternative such as a CMOS camera [18]. Beyond improved bandwidth, the use of a photoreceiver also allows higher illumination intensities, increasing the signal-to-noise of the microscope.

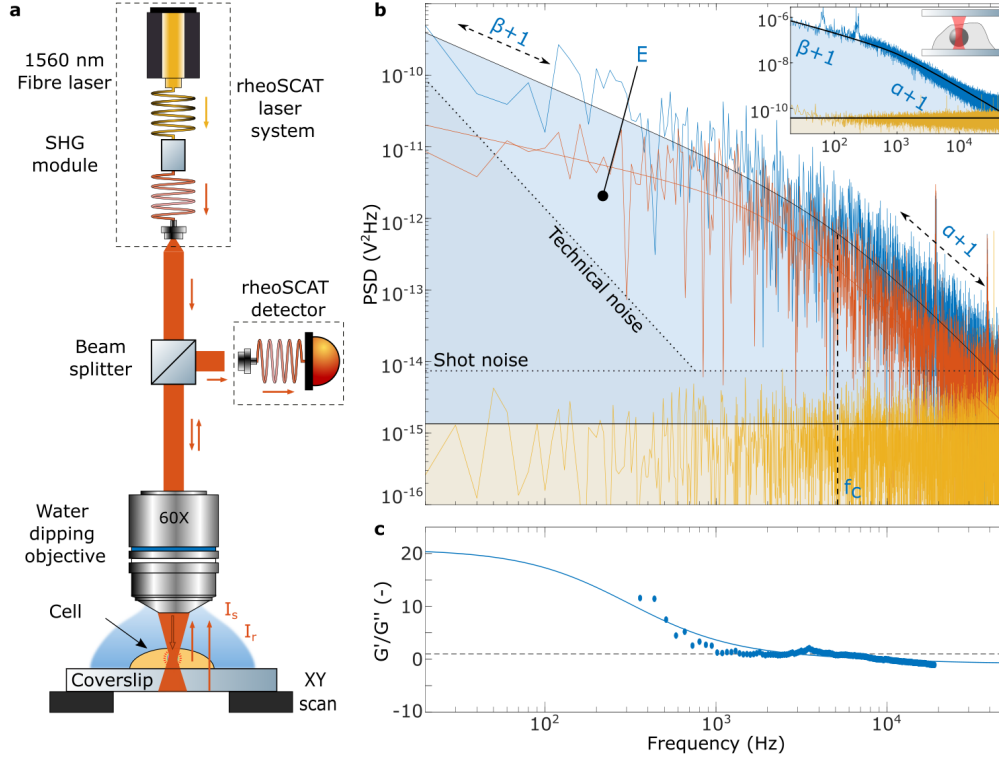


Fig. 1. Experimental setup. **a** Schematic of the rheoSCAT microscope. **b** Power spectral density (PSD) of the photocurrent time traces of pixels situated inside the cell sampled (blue), outside an HeLa cell (red). The yellow curve represent the electronic noise of the microscope. Curves fitting the blue and red PSDs using the two slopes model $S(f)$ are displayed in black and red solid lines. rheoSCAT parameters E , α and f_c are displayed for the blue trace. The dashed lines represent the optical technical and shot noise on the measurement and the horizontal solid line the mean of the electronic noise. Inset: PSD of 1 μm bead embedded inside a HeLa cell and trapped with and optical tweezers exhibiting similar spectral characteristics then the rheoSCAT measurements. **c** Ratio of the elastic (G') and viscous (G'') modulus over frequency calculated from the PSD of the pixel inside the cell (blue). Data points are extracted from the local slope of the blue PSD and the blue curve is calculated from the fitting curve of the blue PSD. Dashed line represents $G'/G'' = 1$.

In a key innovation to suppress light noise, we develop an ultra-low noise microscope illumination source at a wavelength of 780 nm. This is based on a narrow linewidth telecom-wavelength fibre laser (NKT: Koheras ADJUSTIK X15, 1560 nm), as illustrated in Fig. 1a with sub-100 Hz linewidth, several orders of magnitude beneath that of typical iSCAT and other types of phase contrast microscopy illumination sources [18]. The 1560 nm light is then frequency

doubled to 780 nm using a periodically poled nonlinear waveguide, preserving the low-noise characteristics of the original fibre laser while allowing operation in the biologically safe first near-infrared window. The narrow linewidth greatly reduces optical phase noise allowing fainter signals to be detected.

The laser is focused on the sample using a water-dipping objective with 60X magnification and a numerical aperture of 1.0. Using a water dipping objective reduces the number of optical interfaces that the light must traverse, minimising spurious interference and maximising detection efficiency. The output field is collected through the same objective and spatially filtered through a single-mode optical fibre to capture only the scattered and reflected fields from the laser's focal point, following a confocal approach [22]. This suppresses noise from out-of-focus light and higher-order spatial modes.

We detect the spatially filtered output field of the microscope with a 200 kHz bandwidth photodetector that can handle optical powers as high as 10 mW, far above the maximum that can typically be used with a CMOS camera. The photodetector has noise-equivalent power of $0.25 \text{ pW}/\sqrt{\text{Hz}}$ (Newport model 2001-FS-M), allowing shot-noise limited performance even at detected powers as low as 110 pW.

Label-free microrheology at high bandwidth

In a first set of experiments, we use the rheoSCAT microscope to probe the energetics of local regions of a cervical cancer HeLa cell. HeLa cells are cultured in an incubator for 48 hours, followed by plating on a 20 mm×20 mm coverslip for an additional 48 hours, achieving approximately 50% confluence. This allows for the study of individual cells and the medium around them.

We use 13 mW of illumination light, detecting around 160 nW of light reflected from the microscope slide and scattered from the specimen. To analyse the detected signal, we apply Fourier analysis to compute its power spectral density (PSD). Typical PSDs are shown in Fig. 1b.

The observed rheoSCAT signals (blue and red traces) are far higher than the electronic noise (yellow trace) which is roughly a factor of ten below the optical shot noise level (dashed horizontal line), ensuring it has minimal influence on the measurements. Inside the cell (blue trace), at low frequencies where the activity is largest, the rheoSCAT signals exceed the optical shot noise by about six orders of magnitude. Notably, even though the activity level drops rapidly with increasing frequency, the signal remains resolvable above the shot noise up to frequencies as high as 50 kHz. This both enables analysis of high frequency bioactivity signals and the possibility of fast data acquisition. The spatial resolution of the measurements is far-sub-cellular, approximately 400 nm, determined by the tight focusing of the laser light. The strong signal observed within the cell stem from the motion of endogenous scatterers in the cellular cytoplasm, driven by cytoskeleton fluctuations. They likely stem from correlated motion of proteins and proteins complexes rather than larger constituents such as mitochondria (see Supplementary Information). We confirm that it is not attributable to laser noise through separate measurements on a sample without cell, which showed significant lower fluctuations with different character as shown by the dashed line in Fig. 1b (see Supplementary Information).

Outside the cell (red trace) but in its proximity, a strong signal is also observed around four orders of magnitude above the shot noise level at low frequencies. This is attributed to the cellular secretome, which has previously been visualized using iSCAT detection [23], as well as to movements of particles in the surrounding fluid.

The PSD observed within the cell exhibit spectral features consistent with probe-based microrheological measurements of cellular materials [5–7]. These features reflect the material's viscoelastic properties, which display soft glassy behaviour [6]. At low frequencies, elasticity dominates and mechanical energy is stored; at high frequencies, viscosity dominates, leading to energy dissipation [5–7]. This gives rise to a frequency-dependent complex shear modulus

$G^*(f) = G'(f) + iG''(f) = A(if)^\alpha + B(if)^\beta$ characterized by a double power-law behaviour [5–7], where G' and G'' are the storage and loss moduli, $i^2 = -1$, A and B are constants and the exponents α and β correspond to the viscous and elastic regimes, respectively. This complex modulus can be related to the motional power spectral density $S(f)$, using the fluctuation dissipation theorem [24]: $S(f) \propto \frac{1}{f} \text{Im} \left[\frac{1}{G^*} \right]$. This gives an analytic expression for $S(f)$ as function of A , B , α and β (see Supplementary Information) that can be used to fit the experimental PSD and provides four independent rheoSCAT microscopy parameters.

the viscous and elastic exponents α and β provide information about the local rheological properties of the cell. As in typical iSCAT measurements or optical tweezers-based particle tracking, they can also be interpreted in terms of diffusive behaviour: $\alpha = 1$ corresponds to normal Brownian diffusion, $\alpha > 1$ indicates super-diffusion driven by active processes, and $\alpha < 1$ reflects sub-diffusion, often arising from viscoelastic constraints or crowding effects [25]. We reparametrize A and B to more physically relevant parameters, E and f_c . We term the parameter E , defined as the integral $E = \int_{f_l}^{f_h} \frac{PSD(f)}{\langle i \rangle} df$, the *energy* parameter since it quantifies the power contained in the detected photocurrent between our chosen cut-off frequencies $f_l = 20$ Hz and $f_h = 50$ kHz, and is related to the local motional energy within the sample. We normalise to the mean photocurrent $\langle i \rangle$ to correct for variations in $\langle i \rangle$ across the specimen. f_c is the *viscoelastic crossover frequency*, defined as $f_c = \exp\left(\frac{\log(B) - \log(A)}{\alpha - \beta}\right)$ [5], which characterises the transition between low-frequency elastic behaviour and high frequency viscous behaviour. A higher viscoelastic crossover frequency signifies increased stiffening, a more solid-like response, and rapid mechanical relaxation, whereas a lower f_c indicates a more fluid-like, compliant response with slower mechanical relaxation. These characteristics can be linked to the properties of the cytoskeletal network and the cells energetic state [5].

Fits of the model to the example PSDs in Fig. 1b (black and red solid lines) show strong agreement with experimental data. To confirm that the observed spectral features reflect cellular rheology, we performed, in parallel, passive microrheology experiments using optical tweezers with a $1 \mu\text{m}$ bead embedded inside a HeLa cell, see Fig. 1b inset. These exhibit a similar double power-law behaviour, with elastic and viscous exponents values comparable to those measured by rheoSCAT, confirming that rheoSCAT captures intrinsic rheological properties without the need for external probes (see Supplementary Information).

While the PSD in our measurements is not calibrated in absolute displacement units (m^2/Hz) due to the unknown detailed properties of the intracellular scatterers, the ratio of the elastic (G') and viscous (G'') moduli can still be extracted. G'/G'' quantify the relative contribution of elasticity and viscosity of the cellular material properties. It is given by (see Supplementary Information):

$$\frac{G'}{G''} = \frac{A f^\alpha \cos(\pi\alpha/2) + B f^\beta \cos(\pi\beta/2)}{A f^\alpha \sin(\pi\alpha/2) + B f^\beta \sin(\pi\beta/2)}. \quad (2)$$

Figure 1c shows the modulus calculated from the PSD in Fig 1b along with the model of Eq. 2 calculated from the fitting parameters. At low frequencies, the cellular response is predominantly elastic, with G' exceeding G'' by up to a factor of 20. At the crossover frequency $f_c = 5$ kHz, the ratio approaches unity, indicating a balanced viscoelastic response. Above f_c , the behaviour becomes increasingly viscous, with the ratio G'/G'' approaching zero. This frequency dependent behaviour is expected for the viscoelasticity of the cytoplasm.

rheoSCAT imaging

Each of the four rheoSCAT parameters can be spatially mapped across the sample to generate multiparameter rheological images. This is achieved by raster scanning the sample in two dimensions with a high-precision nanostage. Doing this, we acquire 50×50 pixel images, covering a $25 \mu\text{m} \times 25 \mu\text{m}$ field of view in less than 2.5 minutes.

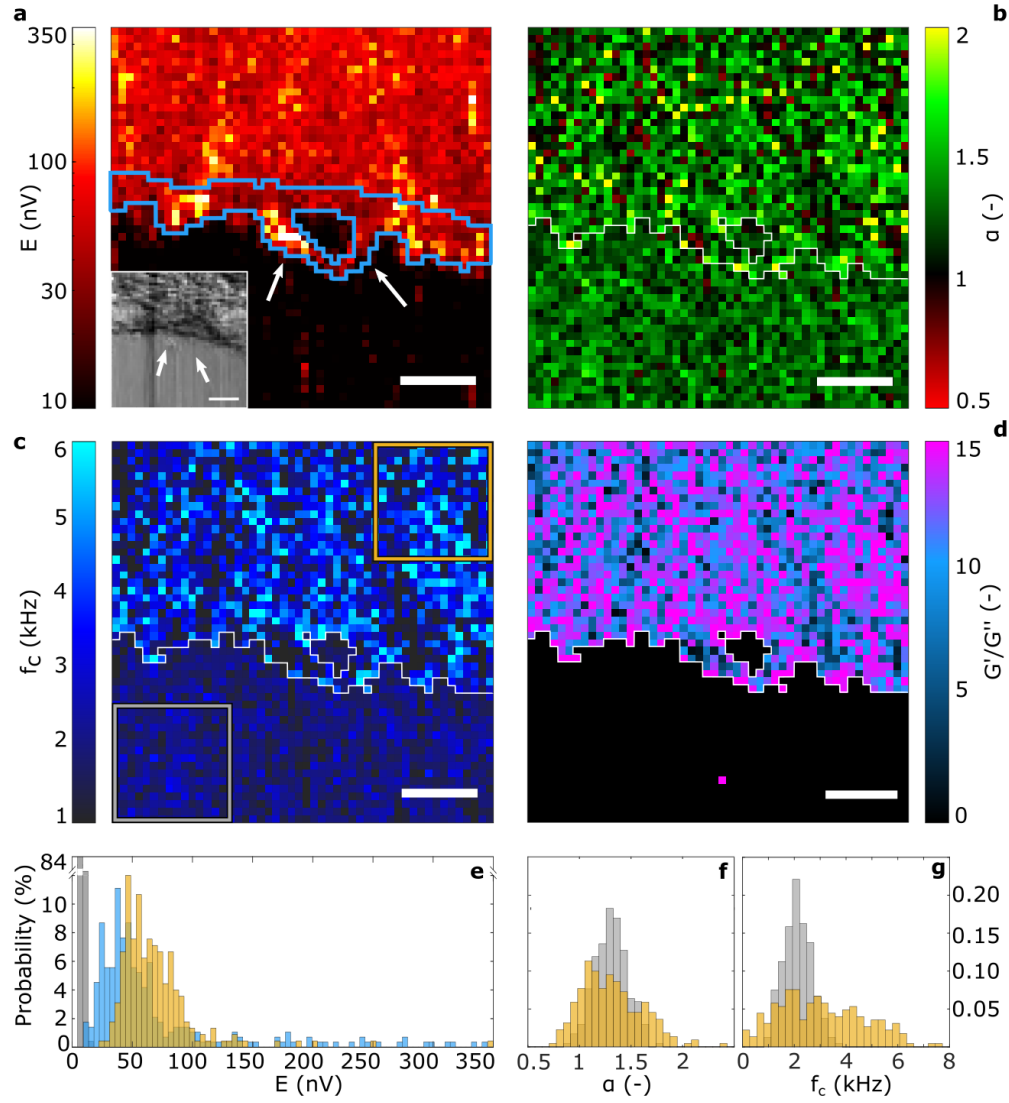


Fig. 2. **rheoSCAT images of cellular energetics.** **a**, **b**, **c** and **d** images of the energy E , the viscous exponent α , the crossover frequency f_c , and the modulus ratio G'/G'' averaged over low frequencies for a portion of a HeLa cell. The blue contour in **a** highlight the cellular membrane region. The white line in **b**, **c** and **d** separates the intra- and extracellular regions. The inset in **a** represents the corresponding mean intensity image, calculated by taking the average photocurrent, $\langle i \rangle$, over a 50 ms measurement period for each pixel and plotted against pixel position. **e-g** histograms of the energy, viscous exponent and crossover frequency parameter, respectively in different region of the sample. Yellow: within the cell; grey: outside the cell; and blue: within the cell membrane region. The pixels used to generate the histograms are shown in **c** by the regions bounded with the corresponding colour. All histograms are normalized such that they sum to 1. Scale bars represent 5 μm .

Imaging HeLa cells, we find that fits to the elastic exponent (β) are inaccurate for some pixels due to the small number of low-frequency data points. For pixels that clearly show the

low-frequency slope, we find that an average elastic exponent value of $\beta = 0.5 \pm 0.005$ inside the cell, and 0.3 ± 0.002 outside that varies by about 20% and 33% respectively across the image. Given the narrow range of observed values, we assume this mean values for the remaining pixels. We then fit E , α , and f_c to generate rheoSCAT parameter images. The uncertainty in the average value is calculated by taking the standard deviation across pixels and calculating the standard error, which is typically below a percent for each parameter (α , β , E , f_c and G'/G''). Therefore, these uncertainties are omitted throughout the remainder of the manuscript.

Example images of E , α , f_c and G'/G'' for a portion of a single HeLa cell are displayed in Figs. 2a-d.

The energy parameter image (Fig. 2a) reveals pronounced contrast between the energy magnitude inside and outside the cell, clearly distinguishing the intra-cellular and extra-cellular environments. Interestingly, it also displays distinct high energy structural patterns within the cellular region concentrated near its boundary (blue contour). These elevated energy regions are likely associated with active surface structures. For instance, the area highlighted by the white arrows in Fig. 2a has shape and size characteristic of a pair of filopodium, which are commonly present on the membrane of HeLa cells [26]. The high E values observed in these regions potentially indicate highly dynamic processes known to occur at the cell edge, such as cortical actin polymerization [27].

The inset of Fig. 2a shows the mean intensity image derived from the same data used to create the energy parameter image. This captures the static phase signal term ($\langle i \rangle$) in Eq. (1), analogous to iSCAT and phase contrast microscopy images. Notably, the contrast is far inferior to that of the energy parameter image. Indeed, the filopodium-like structures observed with high signal-to-noise ratio in the rheoSCAT image are invisible (white arrows in Fig. 2a and inset of Fig. 2d). This highlights a key advantage of rheoSCAT microscopy: by detecting fluctuations rather than mean signals, it can resolve fainter features and achieve substantially higher contrast than conventional static phase imaging techniques.

Unlike the energy parameter image, the viscous exponent α parameter image (Fig. 2b) shows little large-scale structure and the same mean value inside and outside the cell of $\alpha = 1.2$. This value is consistent with reported ranges [5–7] and suggests that the spatially-average short-time diffusion is close to normal in both regions. There are significant differences in α inside and outside the cell but they are exhibited in the spatial fluctuations rather than the mean. We analyse these later.

Like the energy parameter, the crossover frequency parameter (f_c) reveals a clear contrast between the intracellular and extracellular environments (Fig. 2c), with significantly higher f_c values inside the cell compared to the surrounding medium. While the f_c spatial distribution appears more uniform than the energy parameter, structures ranging from two to five microns are discernible. This was further validated through autocorrelation analysis (see supplementary information). These local spatial variations might reflect underlying differences in cytoplasmic mechanical properties, such as actin filament network organization, the presence of organelles, and even molecular motor dynamics, which are known to operate at these length scales [28].

Fig. 2d displays the average of G'/G'' from 20 Hz to 200 Hz. As expected, the cell exhibits an elastic response at low frequency with average G'/G'' around 10 inside the cell ranging from 20 to 0. Outside the cell, the ratio is dominated by viscosity with G'/G'' around 0 as expected for the surrounding medium.

To quantitatively analyse the rheoSCAT parameters, we computed histograms across the cell regions indicated in Fig. 2c. These are shown in Fig. 2e-g.

The energy parameter histograms (Fig. 2e) show the sharp contrast between the intracellular (yellow) and extracellular (grey) regions, as also observed in the corresponding energy parameter image, with mean values a factor 8.7 larger inside the cell than outside (69 nV c.f. 7.9 nV). The histogram for pixels within the membrane region (blue contour, Fig. 2a), shown in blue in

Fig. 2e reveals two distinct behaviours. First, as expected from the high-activity regions, there is a long high-energy tail extending to values larger than 350 nV. Second, there are regions of low activity, with energy values below 50 nV, significantly lower than those in deeper cell regions. These low-energy pixels appear as dark red areas within the blue contour in Fig. 2a. They likely correspond to thinner areas of the cell, a characteristic commonly seen when cells, particularly cancer cells such as HeLa cells, spread on coverslips. Thinner regions contain fewer cellular components, leading to reduced scattering intensity fluctuations and consequently reduced energy parameter values.

The viscous exponent α histograms (Fig. 2f) show that, while the mean α values inside and outside the cell are similar, there is higher variability within the cell. The variance inside the cell, $\langle \alpha^2 \rangle - \langle \alpha \rangle^2 = 0.022$, is 3.6 times larger than is observed outside, reflecting a broader range of diffusion behaviours within the cellular environment. The cell interior exhibits super-diffusive behaviour ($\alpha > 1$), indicative of active motion or transport processes, as well as sub-diffusive behaviour ($\alpha < 1$), likely caused by chemical binding or cytoskeletal crowding [29]. In contrast, the region outside the cell displays α values closer to 1 over the entire extracellular region, characteristic of normal diffusion.

The average crossover frequency f_c inside the cell (yellow, Fig. 2g) is approximately 3.0 kHz, consistent with values from microrheology measurements reported in the literature [5]. Outside the cell (grey), it is reduced to 2.1 kHz. Additionally, the intracellular distribution shows significantly greater variability, with a variance 9.1 times larger than outside.

Imaging cellular changes

We now assess the capability of rheoSCAT microscopy to monitor changes in the state of cells over time. To achieve this, we image an A549 lung carcinoma epithelial cell before (Fig. 3a) and after (Fig. 3b) ten minutes of exposure to 2% paraformaldehyde (PFA). We also image a different A549 cell from the same sample twenty four hours post-treatment (see methods and supplementary information). As a chemical fixative, PFA stabilizes cellular structures by forming covalent bonds between side chains of amino acids, increasing membrane permeability, and ultimately inducing cell death [30].

The rheoSCAT images show striking differences due to the action of PFA after only ten minutes. By contrast, the mean intensity images reveal only subtle changes (insets, Fig. 3a & b). This demonstrates the rheoSCAT microscope's ability to effectively differentiate between untreated and stressed cells that are morphologically intact, a capability challenging to achieve with conventional microscopy.

Next, we examine how each individual rheoSCAT parameter contributes to these observed differences following PFA treatment.

The energy parameter shows a dramatic reduction after PFA treatment across the entire cellular region that is imaged, with mean dropping by a factor of 2 from 60 nV (yellow, Fig. 3c) to 30 nV (green). Twenty-four hours after PFA treatment, the energy parameter drops further to 7 nV, similar to background levels (12 nV, light and dark grey) and indicating that the cell activity is completely suppressed (see supplementary information).

The elastic exponent α changes markedly within the first micron of the cell membrane, as shown by the red diagonal band in Fig. 3b, indicating a change from super-diffusion ($\alpha=1.3$) prior treatment to sub-diffusion ($\alpha=0.8$) afterwards (pink, Fig. 3d). This aligns with the expected effects of PFA, which cross-links biomolecules and restricts the motion of cellular constituents, shifting their dynamics toward sub-diffusion. Away from the cell membrane, no significant changes in α are seen. These observations are consistent with fixation assault near the membrane. This process induces a global stressed state, as shown by the energy parameter images, but only locally changes its mechanical properties. This was confirmed by the images taken twenty four hours post-fixation treatment, where the entire cell exhibits sub-diffusion $\alpha=0.7$, indicating

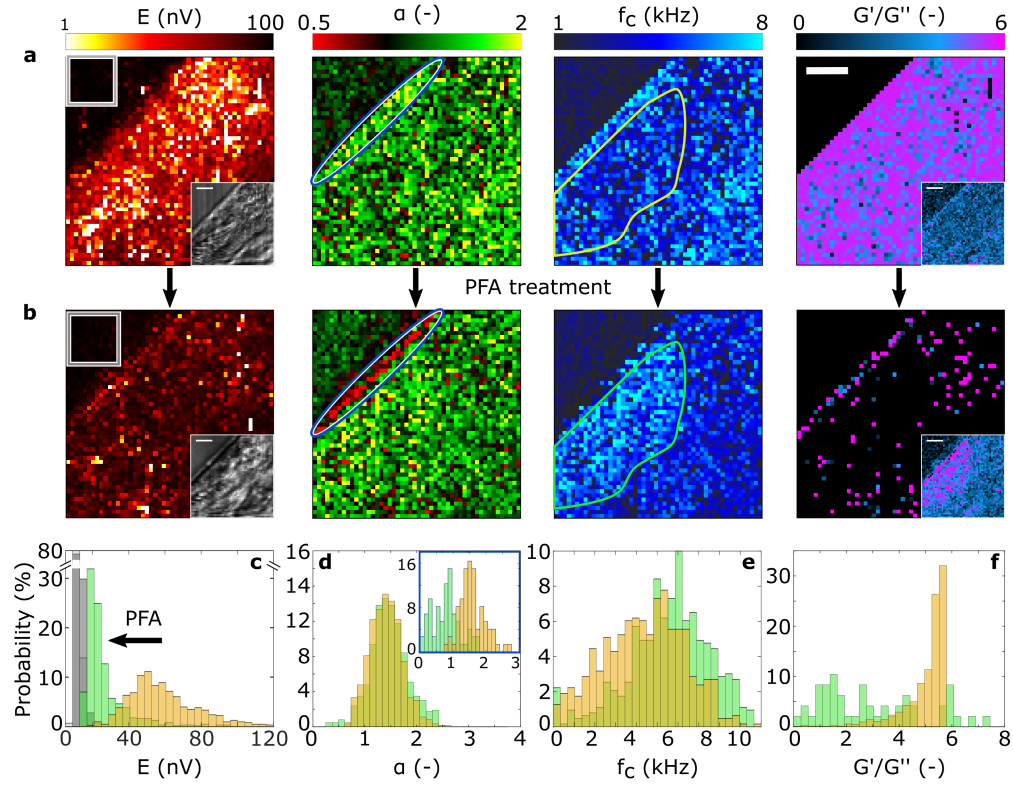


Fig. 3. **rheoSCAT parameters evolution.** **a** rheoSCAT parameter images of a region of a untreated A549 cell. **b** rheoSCAT parameter images of the same cell region 10 minutes after PFA treatment. In both **a** and **b**, from left to right, the images represent E , α , f_c and G'/G'' at low frequency (around 100 Hz). The insets in the E images are the corresponding mean intensity images and the insets in G'/G'' represent the average of G'/G'' at high frequencies (around 10 kHz) **c-f** histograms of the energy, α , f_c and G'/G'' , respectively, in different regions of the sample. Yellow: within the untreated cell; green: within the PFA-treated cell; light grey: outside the healthy cell; dark grey: outside PFA-treated cell; and pink: within the first micron of the PFA-treated cell. The pixels used to generate the histograms are shown by the regions bounded with the corresponding colour. All histograms are normalized so that they sum to 1. All scale bars represent $5 \mu\text{m}$, with the top-right scale bar applicable to all the images with the same size in **a** and **b**.

complete fixation (see supplementary information).

The viscoelastic crossover frequency (f_c) exhibits a localized increase from 4 kHz (yellow, Fig. 3e) to 6 kHz (green) within a spatial region extending approximately 8 microns from the cell membrane (green contour, Fig. 3b). This increase may be due to local stress responses that alter the mechanical properties of cellular components. Potential contributing factors include osmotic and macromolecular crowding effects [29], cytoskeletal remodeling such as microtubule buckling or collapse [31], and membrane permeabilization processes that alter cellular viscosity [32].

Outside this region, the average f_c value reduces from 5 kHz to 4 kHz, mirroring the global reduction observed in the energy (E) parameter image. After 24 hours, f_c has drastically decreased across the entire cell region to an average f_c value of 20 Hz, well below the values observed in untreated cells. This substantial drop suggests a complete loss of cytoskeletal integrity and

membrane mechanical properties, marking the final stages of cellular degradation.

The ratio G'/G'' at low frequencies (Fig. 3a and b right) shows a marked reduction following PFA treatment, mirroring the changes observed in the energy parameter images. This decrease likely reflects the cessation of cellular activity: the cell no longer responds, intracellular motion is suppressed, and its mechanical behaviour becomes more fluid-like. This suggests that the cell's elastic response is primarily governed by active processes and internal motion rather than passive structural components. Interestingly, at high frequencies (Fig. 3a and b right inset) the G'/G'' ratio reveals the opposite trend (see insets). In this regime, the cell exhibits increased stiffness, with a higher ratio, particularly in regions where the viscoelastic crossover frequency f_c also increases. This is consistent with a passive stiffening response to PFA fixation.

Discussion

Label-free imaging techniques such as iSCAT and ROCS have recently begun to be used to measure cellular activity [9–11]. rheoSCAT's ability to observe the cytoskeleton's elastic-to-viscous crossover, enabled by a twenty-fold increase in acquisition speed, connects this observed activity to microrheology. This is significant because viscoelasticity modulates cell health and function [1], yet has traditionally only been measurable using spatially coarse-grained methods such as optical tweezers [5, 6, 33] or multi-particle tracking experiments that follow the independent trajectories of an ensemble of fluorescent labels [4] or nanoparticles [19]. In contrast, rheoSCAT enables direct, unlabeled imaging of viscoelasticity over large regions of live cells, simultaneously capturing both mechanical properties and activity levels. This allows rheological mapping with higher spatial resolution, faster acquisition, and simpler instrumentation than existing techniques.

Whereas conventional microrheology typically relies on externally introduced probe particles [8, 19], rheoSCAT exploits scattering from endogenous particles within the cytoplasm. It yields power spectral densities that are consistent with previous microrheology measurements [5–7], α and f_c parameters consistent with the microrheology literature [5–7], and fixation-induced changes that align with expectations. A key question is why the complex, heterogeneous ensemble of particles in the cytoplasm can yield results consistent with established rheological measurements. The likely explanation lies in correlated motion among particles, which is known to occur across length scales comparable to the size of our microscope voxel [33, 34].

Since the intensity of dipole scattering scales as the sixth power of particle radius, one might expect large structures like mitochondria to dominate the rheoSCAT signal. However, we observe rheoSCAT spectra consistently at all pixels within the sampled cell. This implies that the dominant scattering elements are abundant and spatially continuous – excluding sparse, larger structures as the primary contributors. Instead, the signal must arise from smaller, higher abundance and more weakly scattering particles. The existence of correlated motions explains how this can occur. Particles in the cytoplasm undergo partially coherent motion driven by cytoskeletal dynamics, superimposed with random local fluctuations [33, 34]. The rheoSCAT power spectrum includes contributions from both types of motion. Crucially, the relative contribution from correlated motions increases linearly with particle number due to the presence of cross-correlation terms that are absent for purely random motions (see Supplementary Information). As a result, our estimates show that, due to their overwhelming abundance, correlated motion from proteins and protein complexes is likely the primary signal source (see Supplementary Information). That the microscope is sensitive to protein motions is consistent with iSCAT's demonstrated ability to detect individual proteins [18] and to observe fluctuations due to their motions within the nucleus [35].

The dominance of correlated protein motions, driven by cytoskeleton dynamics, indicates that rheoSCAT measurements probe the bulk viscoelasticity across the microscope voxel rather than local diffusive motion, explaining the agreement with models of cytoskeletal viscoelasticity.

This new understanding may also help explain the biophysical basis of activity signals previously observed with ROCS [9] and iSCAT [12].

We have shown that rheoSCAT can extract detailed, spatially resolved information about the material properties and activity of cells, including overall activity levels, diffusion and the ratio of storage and loss moduli as a function of frequency ($G'(f)/G''(f)$). An outstanding question is whether it is possible to achieve an absolute calibration the complex shear modulus. Typically, such calibration requires detailed knowledge of the size and shape of the probe particles [24]. It is conceivable that the ensemble of cytoplasmic proteins that contribute to the rheoSCAT signal is sufficiently uniform, within a given cell type, to permit such a calibration. Alternatively, in two-particle microrheology correlated particle motions allow calibration without detailed knowledge of the probe particles [36]. Similar techniques may be applicable to ensembles of correlated particles such as those in rheoSCAT. These remain open questions for future investigation.

A limitation of our current rheoSCAT microscope is its slow acquisition time (2.5 minutes per frame). If only activity above a few kilohertz was of interest, the pixel dwell time could be reduced to beneath a millisecond using two-dimensional acousto-optic modulators (AOM) or resonant scanning [37]. This would reduce the acquisition time for 50×50 pixel images to two seconds. Video rate imaging could be achieved using a wide-field configuration and high-speed camera. This would allow the observation of dynamics down to 20 Hz at the expense of reduced signal bandwidth.

Methods

Cell culture conditions

HeLa (CCL-2) and A549 (CCL-185) were maintained in Dulbecco's Modified Eagle Medium (DMEM) supplement with 10% foetal bovine serum (FBS), 2mM L-glutamine and 100 units/ml penicillin/streptomycin in a humidified 37 degree incubator supplement with 5% CO₂.

PSD fits

To enhance the accuracy and reproducibility of the PSD fits, the analysis was performed on a logarithmic scale. Data points above 15 kHz were excluded from the fitting process to minimize the impact of high-frequency noise artifacts, including the distinct noise peaks observed at 19 and 38 kHz. This approach allowed us to focus on the most informative frequency ranges and avoid biases that could arise from less reliable high-frequency data.

Cell fixation

To conduct the cell fixation experiment, the sample medium was carefully partially removed using a pipette, ensuring that the microscope alignment remained undisturbed. The medium was then replaced with a fresh solution supplemented with 2% PFA. Imaging was resumed 10 minutes after the introduction of the PFA solution to allow sufficient time for the fixation process to initiate. Following initial measurements, the sample was removed from the microscope and stored overnight in a sterile environment at room temperature. After twenty four hours of PFA treatment, the same sample was re-mounted and re-imaged to assess the long-term fixation effects.

Funding. This work was primarily supported by the Air Force Office of Scientific Research (grant no. FA9550-22-1-0047 and FA9550-24-1-0286). It was also supported by the Australian Research Council Centre of Excellence in Quantum Biotechnology (grant no. CE230100021).

Acknowledgments.

Some of the cells used in this research were derived from a HeLa cell line. Henrietta Lacks, and the HeLa cell line that was established from her tumor cells without her knowledge or consent in 1951, have

made significant contributions to scientific progress and advances in human health. We are grateful to Henrietta Lacks, now deceased, and to her surviving family members for their contributions to research.

The author acknowledges HC Photonics for the discount on the second harmonic generator module, which contains the periodically poled nonlinear waveguide used for converting 1560 nm light to 780 nm.

Ethics declarations. The authors declare no conflicts of interest.

Data Availability Statement. The data supporting the findings of this study are available within the paper and its Supplementary Information. All other data that support the findings of this study are available from the corresponding author on request.

Supplemental document. See Supplement for supporting content.

References

1. M. R. Mofrad, "Rheology of the cytoskeleton," *Annu. Rev. Fluid Mech.* **41**, 433–453 (2009).
2. F. Gittes, B. Schnurr, P. Olmsted, *et al.*, "Microscopic viscoelasticity: shear moduli of soft materials determined from thermal fluctuations," *Phys. Rev. Lett.* **79**, 3286 (1997).
3. L. Chevry, R. Colin, B. Abou, and J.-F. Berret, "Intracellular micro-rheology probed by micron-sized wires," *Biomaterials* **34**, 6299–6305 (2013).
4. T. P. Kole, Y. Tseng, and D. Wirtz, "Intracellular microrheology as a tool for the measurement of the local mechanical properties of live cells," in *Methods in Cell Biology*, vol. 78 (Elsevier, 2004), pp. 45–64.
5. A. Rigato, A. Miyagi, S. Scheuring, and F. Rico, "High-frequency microrheology reveals cytoskeleton dynamics in living cells," *Nat. Phys.* **13**, 771–775 (2017).
6. L. Chaubet, A. R. Chaudhary, H. K. Heris, *et al.*, "Dynamic actin cross-linking governs the cytoplasm's transition to fluid-like behavior," *Mol. Biol. Cell* **31**, 1744–1752 (2020).
7. B. D. Hoffman, G. Massiera, K. M. Van Citters, and J. C. Crocker, "The consensus mechanics of cultured mammalian cells," *PNAS* **103**, 10259–10264 (2006).
8. P.-H. Wu, C. M. Hale, W.-C. Chen, *et al.*, "High-throughput ballistic injection nanorheology to measure cell mechanics," *Nat. Protoc.* **7**, 155–170 (2012).
9. F. Jünger, D. Ruh, D. Strobel, *et al.*, "100 Hz rocs microscopy correlated with fluorescence reveals cellular dynamics on different spatiotemporal scales," *Nat. Commun.* **13**, 1758 (2022).
10. Y.-T. Hsiao, T.-Y. Wu, B.-K. Wu, *et al.*, "Spinning disk interferometric scattering confocal microscopy captures millisecond timescale dynamics of living cells," *Opt. Express* **30**, 45233–45245 (2022).
11. A. Trelin, S. Kussauer, P. Weinbrenner, *et al.*, "Chiscat: Unsupervised learning of recurrent cellular micromotion patterns from a chaotic speckle pattern," *Nano Lett.* **24**, 12374–12381 (2024).
12. Y.-T. Hsiao, I.-H. Liao, B.-K. Wu, *et al.*, "Probing chromatin condensation dynamics in live cells using interferometric scattering correlation spectroscopy," *Commun. Biol.* **7**, 763 (2024).
13. C. Joo, C. L. Evans, T. Stepinac, *et al.*, "Diffusive and directional intracellular dynamics measured by field-based dynamic light scattering," *Opt. Express* **18**, 2858–2871 (2010).
14. Y.-F. Huang, G.-Y. Zhuo, C.-Y. Chou, *et al.*, "Coherent brightfield microscopy provides the spatiotemporal resolution to study early stage viral infection in live cells," *ACS Nano* **11**, 2575–2585 (2017).
15. B. Li, S.-X. Dou, J.-W. Yuan, *et al.*, "Intracellular transport is accelerated in early apoptotic cells," *PNAS* **115**, 12118–12123 (2018).
16. P. P. Dzeja and A. Terzic, "Phosphotransfer networks and cellular energetics," *J. Exp. Biol.* **206**, 2039–2047 (2003).
17. H. Kamata and H. Hirata, "Redox regulation of cellular signalling," *Cell. Signal.* **11**, 1–14 (1999).
18. M. Piliarik and V. Sandoghdar, "Direct optical sensing of single unlabelled proteins and super-resolution imaging of their binding sites," *Nat. Commun.* **5**, 4495 (2014).
19. M. Guo, A. J. Ehrlicher, M. H. Jensen, *et al.*, "Probing the stochastic, motor-driven properties of the cytoplasm using force spectrum microscopy," *Cell* **158**, 822–832 (2014).
20. S. Nishiwaki, K. Narumi, and T. Korenaga, "Interference phase-contrast imaging technology without beam separation," *Sci. Reports* **9**, 1753 (2019).
21. N. Mauranyapin, L. Madsen, M. Taylor, *et al.*, "Evanescent single-molecule biosensing with quantum-limited precision," *Nat. Photonics* **11**, 477–481 (2017).
22. T. Dabbs and M. Glass, "Single-mode fibers used as confocal microscope pinholes," *Appl. Opt.* **31**, 705–706 (1992).
23. M. P. McDonald, A. Gemeinhardt, K. König, *et al.*, "Visualizing single-cell secretion dynamics with single-protein sensitivity," *Nano Lett.* **18**, 513–519 (2018).
24. R. Brau, J. Ferrer, H. Lee, *et al.*, "Passive and active microrheology with optical tweezers," *J. Opt. A: Pure Appl. Opt.* **9**, S103 (2007).
25. N. Gal and D. Weihs, "Experimental evidence of strong anomalous diffusion in living cells," *Phys. Rev. E Stat. Nonlinear, Soft Matter Phys.* **81**, 020903 (2010).
26. A. B. Bohil, B. W. Robertson, and R. E. Cheney, "Myosin-x is a molecular motor that functions in filopodia formation," *PNAS* **103**, 12411–12416 (2006).

27. L. B. Case and C. M. Waterman, "Integration of actin dynamics and cell adhesion by a three-dimensional, mechanosensitive molecular clutch," *Nat. Cell Biol.* **17**, 955–963 (2015).
28. J. Najafi, S. Dmitrieff, and N. Minc, "Size-and position-dependent cytoplasm viscoelasticity through hydrodynamic interactions with the cell surface," *PNAS* **120**, e2216839120 (2023).
29. Q. Bone and E. Denton, "The osmotic effects of electron microscope fixatives," *J. Cell Biol.* **49**, 571–581 (1971).
30. M. C. Jamur and C. Oliver, "Cell fixatives for immunostaining," in *Immunocytochemical methods and protocols*, (Springer, 2009), pp. 55–61.
31. E. M. Tanaka and M. W. Kirschner, "Microtubule behavior in the growth cones of living neurons during axon elongation," *J. Cell Biol.* **115**, 345–363 (1991).
32. R. Cheng, F. Zhang, M. Li, *et al.*, "Influence of fixation and permeabilization on the mass density of single cells: a surface plasmon resonance imaging study," *Front. Chem.* **7**, 588 (2019).
33. J. C. Crocker, M. T. Valentine, E. R. Weeks, *et al.*, "Two-point microrheology of inhomogeneous soft materials," *Phys. Rev. Lett.* **85**, 888 (2000).
34. J. C. Crocker and B. D. Hoffman, "Multiple-particle tracking and two-point microrheology in cells," *Methods Cell Biol.* **83**, 141–178 (2007).
35. M. Mazaheri, K. Kasaian, D. Albrecht, *et al.*, "iscat microscopy and particle tracking with tailored spatial coherence," *Optica* **11**, 1030–1038 (2024).
36. A. J. Levine and T. Lubensky, "One-and two-particle microrheology," *Phys. Rev. Lett.* **85**, 1774 (2000).
37. A. Terrasson, N. P. Mauranyapin, C. A. Casacio, *et al.*, "Fast biological imaging with quantum-enhanced raman microscopy," *Opt. Express* **32**, 36193–36206 (2024).